Journal of Rock Mechanics and Geotechnical Engineering 17 (2025) 20–30

Contents lists available at ScienceDirect

Journal of Rock Mechanics and Geotechnical Engineering

journal homepage: www.jrmge.cn

Qian Lecture

Constraints on triggered seismicity and its control on permeability evolution

Derek Elsworth [a, *], Ziyan Li [a], Pengliang Yu [a], Mengke An [b], Fengshou Zhang [c], Rui Huang [a, c], Zihan Sun [d], Guanglei Cui [d], Tianyu Chen [d], Quan Gan [e], Yixin Zhao [f], Jishan Liu [g], Shimin Liu [a]

[a] Energy and Mineral Engineering & Geosciences, EMS Energy Institute and G³ Center, Pennsylvania State University, University Park, PA, 16802, USA
[b] Hong Kong Polytechnic University, Hong Kong, China
[c] Tongji University, Shanghai, China
[d] Northeastern University, Shenyang, China
[e] Chongqing University, Chongqing, China
[f] China University of Mining and Technology (Beijing), Beijing, China
[g] University of Western Australia, Crawley, Australia

ARTICLE INFO

Article history:
Received 13 September 2024
Received in revised form
26 November 2024
Accepted 27 November 2024
Available online 7 December 2024

Keywords:
Seismicity
Dilatant hardening
Critical stiffness
Maximum seismic moment
Permeability change

ABSTRACT

Triggered seismicity is a key hazard where fluids are injected or withdrawn from the subsurface and may impact permeability. Understanding the mechanisms that control fluid injection-triggered seismicity allows its mitigation. Key controls on seismicity are defined in terms of fault and fracture strength, second-order frictional response and stability, and competing fluid-driven mechanisms for arrest. We desire to constrain maximum event magnitudes in triggered earthquakes by relating pre-existing critical stresses to fluid injection volume to explain why some recorded events are significantly larger than anticipated seismic moment thresholds. This formalism is consistent with several uncharacteristically large fluid injection-triggered earthquakes. Such methods of reactivating fractures and faults by hydraulic stimulation in shear or tensile fracturing are routinely used to create permeability in the subsurface. Microearthquakes (MEQs) generated by such stimulations can be used to diagnose permeability evolution. Although high-fidelity data sets are scarce, the EGS-Collab and Utah FORGE hydraulic stimulation field demonstration projects provide high-fidelity data sets that concurrently track permeability evolution and triggered seismicity. Machine learning deciphers the principal features of MEQs and the resulting permeability evolution that best track permeability changes – with transfer learning methods allowing robust predictions across multiple eological settings. Changes in permeability at reactivated fractures in both shear and extensional modes suggest that permeability change (Δk) scales with the seismic moment (M) of individual MEQs as $\Delta k \propto M$. This scaling relation is exact at early times but degrades with successive MEQs, but provides a method for characterizing crustal permeability evolution using MEQs, alone. Importantly, we quantify for the first time the role of prestress in defining the elevated magnitude and seismic moment of fluid injection-triggered events, and demonstrate that such MEQs can also be used as diagnostic in quantifying permeability evolution in the crust.

1. Introduction

Induced or triggered earthquakes are not a new phenomenon as they have occurred in many areas of engineering and resource extraction for over a century. Recent compilations (Foulger et al., 2018) contain over 700 events from 1868 to 2016 and include triggering due to filling of surface reservoirs, construction of surface structures, extraction and injection of fluids (groundwater, gas, oil, geothermal fluids), extraction of mass by mining and tunneling and due to rockburst and gas outbursts. In general, the magnitude of such events increases with the size of the disturbance driving the failure with the maximum magnitude of fluid injection, reservoir filling, and mining-induced events all occurring in the range 5.8 <

* Corresponding author.
E-mail address: elsworth@psu.edu (D. Elsworth).

https://doi.org/10.1016/j.jrmge.2024.11.035

$M_w < 8$. These represent a significant hazard with ~80,000 deaths in the 2008 M_w 8 Wenchuan earthquake – possibly triggered by reservoir filling.

Both tectonic and triggered earthquakes occur in the Earth's crust, where accumulated shear stresses exceed fault strength. Tectonic stresses build up over geological time, but triggering can result from small stress perturbations if the fault is critically stressed (McGarr et al., 2002; Ellsworth, 2013). The frequency of induced earthquakes has increased dramatically in the past decade due to industrial-scale fluid injection. Such activities include hydraulic fracturing, enhanced geothermal systems, and wastewater disposal (Shapiro and Dinske, 2009; Horton, 2012; Keranen et al., 2013; Guglielmi et al., 2015; Walsh and Zoback, 2015; Bao and Eaton, 2016; Elsworth et al., 2016). Key triggering mechanisms include: (1) An increase in pore pressure that reduces the effective normal stress and consequently weakens the fault; (2) the presence of a local stress halo amplifying remote shear stresses due to poroelastic effects, resulting in rupture without changing fault strength (Bao and Eaton, 2016; Elsworth et al., 2016); and (3) aseismic slip that transitions to seismic slip as patch size increases (Guglielmi et al., 2015; Yang and Dunham, 2022). The maximum magnitudes of such fluid injection-triggered earthquakes have been substantial. Notable examples include the M_w 5.7 Prague earthquake in 2011 (Keranen et al., 2013), the M_w 5.1 Fairview earthquake in 2016 (Yeck et al., 2016a), the Mw 5.0 Cushing earthquake (McGarr and Barbour, 2017), the M_w 5.8 Pawnee earthquake (Yeck et al., 2016b; Grandin et al., 2017), and the M_w 5.5 Pohang earthquake in 2017 (Grigoli et al., 2018; Westaway and Burnside, 2019).

Importantly, the prerequisites for the triggering and propagation of tectonic or induced earthquakes, as well as other forms of more limited dynamic failures such as rockbursts and gas outbursts, are common. It is through this lens that we will view these events. That is, all such events result from the serial requirements (1) of the failure of a fault, fracture, or intact rock, and (2) that the failure must be velocity-weakening to prevent self-arrest of the rupture. Furthermore, for the dynamic release of strain, (3) the unloading stiffness of the fault/fracture/intact rock must be greater than that of the external loading system, such that the energy in the surrounding area is ejected through the failing fault or feature. Moreover, for fluid-infiltrated media, (4) fault stiffness is additionally influenced by fluid pressures and pressure rates, and (5) fault strength is controlled by drainage state and dilatant hardening. From this perspective, triggered earthquakes, rockbursts, and gas outbursts can be characterized by examining these critical unifying physical controls. This enables the magnitude of the resulting events to be quantified in terms of the perturbation that is applied. In the case of fluid injection-induced events, the scaled injection volume is a useful metric, suitably modulated by pre-existing shear stress.

We can use these concepts to define the maximum moment magnitude anticipated for a given event and thus avoid the inherent risk of damaging earthquakes. However, in some cases, we wish to deliberately induce small earthquakes as a method of generating porosity and permeability in subsurface reservoirs or to precondition or destress rock masses before mining or tunneling. It is hoped that such multiple microearthquakes (MEQs, with $M_w < 2$) will controllably create new porosity and permeability that can be used for the recovery or disposal of liquid fuels, waste, or geothermal fluids. This raises the possibility that MEQs may be diagnostic of permeability changes. Shallow crustal permeabilities diminish exponentially with depth (Manning and Ingebritsen, 1999; Ingebritsen and Manning, 2010; Manga et al., 2012). This results from both fracture permeability being extremely sensitive to increasing stress (Pearson, 1981) and the impact of rapid healing and sealing of small aperture features (Olsen et al., 1998; Yasuhara, 2004; Im et al., 2018; Hunfeld et al., 2020). Stimulation of the subsurface for energy or fuel recovery typically involves reactivation of existing fractures in shear (Majer et al., 2007) or extension (McClure and Horne, 2014) – each mode of hydraulic-shearing or hydraulic-fracturing, respectively, driven by intentionally elevated fluid pressures. MEQs typically accompany such fractures, offering the potential for MEQs to be diagnostic of the permeability change.

From this perspective, earthquakes ranging from small to large, and triggered either intentionally or naturally, all conform to the same common controls. Thus, we document and then explain these common controls before using them to explore two important issues in contemporary earthquake physics. These are understanding the maximum seismic moment anticipated in fluid injection-triggered earthquakes, and defining the impact of typically smaller but intentionally triggered events in inducing permeability.

2. Natural and induced seismicity

Both natural tectonic and induced earthquakes rely on a sequence of critical triggering processes. Shear stresses must build up, or strength must decrease sufficiently for failure to occur (Elsworth et al., 2016; Candela et al., 2017). Once failure occurs, it must be unstable, i.e. velocity or strain weakening, so that it does not self-arrest. These two characteristics are necessary but insufficient for a dynamic event. In addition, the stiffness of the surrounding medium must be lower than that of the fault or rupturing element – this is equally true in rockbursts and gas outbursts that are unified by this concept. Finally, conditions during slip must be sufficiently advanced so that processes such as dilatant hardening in fluid-saturated media cannot arrest the rupture.

2.1. Strength

Fault strength is typically defined in terms of second-order changes in friction with displacement in terms of rate-state behavior (Dieterich, 1979; Ruina, 1983; An et al., 2022). The coefficient of friction (μ) is calculated as

$$\mu = \mu_0 + a \ln\left(\frac{v}{v_0}\right) + b \ln\left(\frac{v_0\theta}{d_c}\right) \tag{1}$$

where v represents the initial shear velocity, μ_0 is the coefficient of friction at the reference shear velocity v_0 ($v > v_0$), the coefficients a and b describe the direct and evolutionary effects of the change in shear velocity; d_c is a critical shear displacement when reaching a new steady state and is associated with the average lifespan of grain/asperity contacts, and θ is the state variable. The state variable evolves as described by the Dieterich (aging) law (Dieterich, 1979) as

$$\frac{d\theta}{dt} = 1 - \frac{v\theta}{d_c} \tag{2}$$

or the Ruina (slip) law (Ruina, 1983) as

$$\frac{d\theta}{dt} = -\frac{v\theta}{d_c}\ln\left(\frac{v\theta}{d_c}\right) \tag{3}$$

with the idealized response shown in Fig. 1.

2.2. Frictional stability

The parameter $a - b$ partially determines the frictional stability.

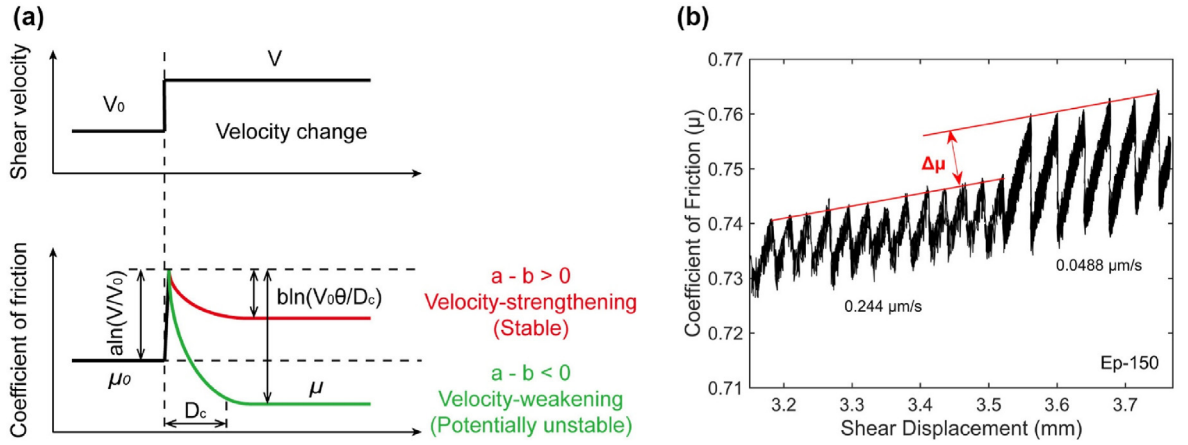

Fig. 1. (a) Rate-state friction response to an increase in shear velocity defining velocity weakening (green) and velocity strengthening (red) modes; and (b) Definition of change in friction coefficient $\Delta\mu$ during stick-slip sequences. Individual sawteeth represent single stick-slips (MEQs) at constant load point velocity shearing and offset in $\Delta\mu$ increase in friction coefficient for a change in shear velocity (after An et al., 2022).

From Eq. (1), at steady state friction, $d\theta/dt = 0$, and thus we have

$$a - b = \Delta\mu_{ss}/\Delta\ln v \tag{4}$$

Eq. (4) indicates that this parameter is defined by the difference in steady-state friction ($\Delta\mu_{ss}$) before and after a velocity step. A positive $a - b$ value indicates that friction increases with shear velocity, which is indicative of velocity-strengthening and represents inherently stable (aseismic) fault slip. A negative $a - b$ value indicates decreasing friction with shear velocity, which is indicative of velocity-weakening and promotes unstable and seismic fault slip – if requirements for critical stiffness (K_{cr}) are also met.

2.3. Critical stiffness

Fault critical stiffness can be indexed by simple spring-slider models. Response is defined in terms of the mass m of the sliding block of such a spring-slider model as

$$K_{cr} = \frac{(b-a)\sigma_n}{d_c}\left(1 + \frac{mv^2}{\sigma_n a d_c}\right) \tag{5}$$

where $(b-a)\sigma_n$ defines the stress drop at failure, and d_c is the length over which this strength drop occurs for the drained but inertial case. Dynamic fault instability can occur if the host loading stiffness K is smaller than the critical stiffness K_{cr}, i.e. $K \leq K_{cr}$ (Gu et al., 1984). For a fault of length l, this geometric stiffness is of the order of $K = G/l$, where G represents the shear modulus. Thus, as the size of the slipping patch, l, increases, the geometric stiffness of the active fault decreases and an aseismic event can transition to a seismic event.

Such analyses are based on simple spring-slider models (Fig. 2), where strength and stiffness are co-linear and act in series. In its simplest form, the slider has a mass and is acted upon by the spring that is stretched by a load point moving at a constant velocity. The load point represents a tectonic shortening (idealized by lengthening of the spring) that increases the extensional stress in the spring and thus increases the shear stress at the base of the slider. When the basal shear strength is exceeded, the slider slips, and the strain energy stored in the spring is released at a rate controlled by the inertia of the slider. This simple analog faithfully represents the role of inertia in controlling the rate of strain energy release around tectonic faults, as controlled by the contrast in stiffness of the loading system (K) and that of the fault (K_{cr}).

The simple spring-slider model (Fig. 2) accommodates the principal features defining seismic slip – the failure must be velocity-weakening and the loading stiffness must be smaller (softer) than the fault stiffness. The failure is dynamic only if the necessary condition of velocity-weakening is met. However, this is insufficient, as the loading stiffness must also be lower than that of the contacting fault surfaces for seismic rupture to occur. In reality, the loading/unloading stiffness of the surrounding medium is not a simple spring, but a geometric stiffness given by the length of the fault embedded within an infinite elastic half-space, such that $K = G/l$. Thus, for a constant stiffness of the gouge material or bare contact surfaces comprising the fault (K_{cr}), as the length (l) of the rupturing patch grows, the geometric stiffness of the loading system decreases ($K = G/l$). Thus, knowing the nucleation length of the patch is a critical parameter because it determines when the rupturing fault will transition from aseismic to seismic rupture – with implications for the related seismic hazard. The characterization of this nucleation length (l), and hence the loading stiffness, is therefore a key indicator of the potential for seismic vs. quiescent reactivation.

However, real faults typically contain pore fluids that influence both strength and stiffness. Indeed, the impacts of strength controlled by effective stresses is a key triggering mechanism for fluid injection-triggered seismicity (Rice, 1993; Cueto-Felgueroso et al., 2018; Alghannam and Juanes, 2020) (Fig. 2). This, in turn, can be represented conceptually as a spring-slider with the load point moving at a constant velocity and a drainage state defined for fluids adjacent to the fault. This system geometry (Fig. 2) represents the reactivation of the fault, with a vertically loaded piston that compresses the spring and represents the fault boundary. The fault core is represented by the slider with the vertical spring, an analog to the poro-elastic response of the rock skeleton flanking the fault. Again, the spring-slider defines the combined fault stiffness (geometric stiffness in the spring) and friction in the fault core (slider). The spring stiffness can be recovered from the geometric stiffness of the fault, which is defined as the ratio of the shear modulus of the rock to the length of the slipping patch (G/l) (Ruina, 1983), as noted previously. The shear stress acting on the slider is transmitted from the extensile stress in the spring and is defined by the stretching and the constant of the spring. Initially, both the spring and the slider move at a constant slip rate (v_0) with no relative displacement. Following fluid injection or drainage, the spring length changes with the application of a new constant velocity v_0 of the load point and where the slider velocity, v, changes. Relative

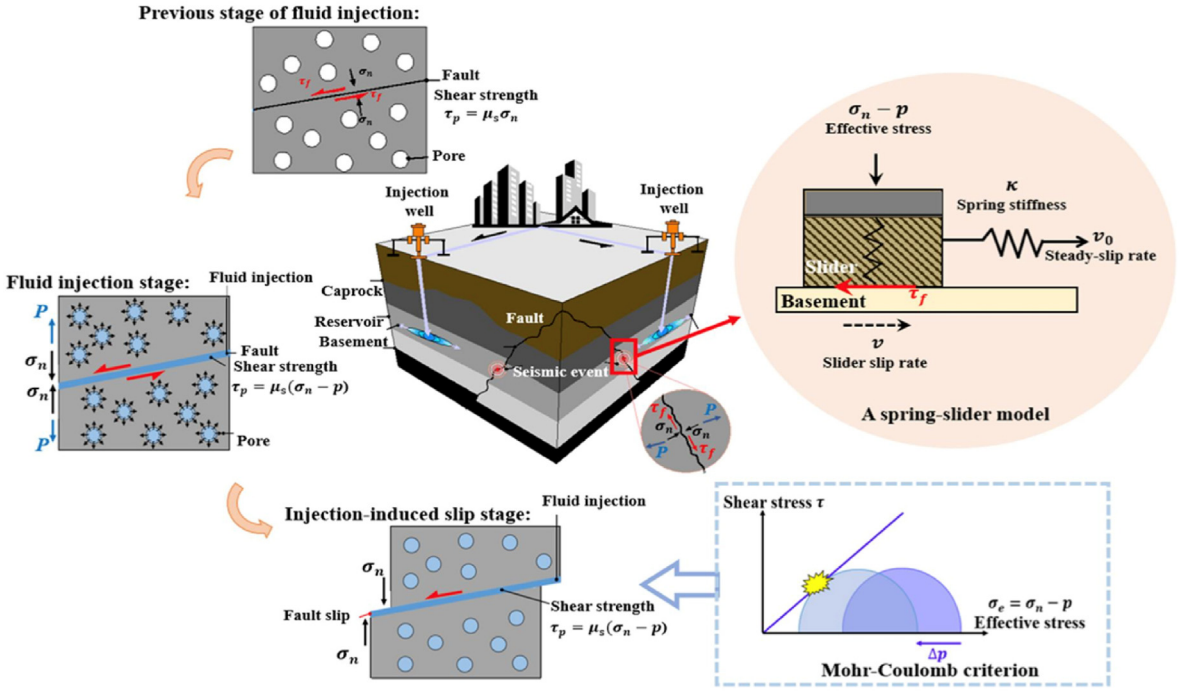

Fig. 2. Physical mechanisms contributing to triggering fault reactivation during injection. τ_p is the peak shear strength, τ_f is the dynamic shear strength. μ_s is the static friction coefficient, σ_n is the normal stress, p is the pore pressure, K is the spring stiffness, and v_0 is the steady-slip rate (after Sun et al., 2024).

displacement between the load point and slider (U) occurs, and $U = 0$ only if $v = v_0$. A key question then remains as to how the fault stiffness evolves with the magnitude and rate of applied fluid pressures. If the contact stiffness transits the threshold $K \approx G/l$, then instability will develop as the slipping patch lengthens. Thus, defining the fault contact stiffness K_{cr} with evolving pore fluid pressure becomes important, as this can drive aseismic fault slip to transition to seismic slip. To this end, a modified critical stiffness can be defined as (Sun et al., 2024):

$$K_{cr} = -\frac{\alpha(\dot{\sigma_n} - \dot{p})}{v_0} + \frac{(b-a)(\sigma_n - p)}{d_c} + \xi\left(\frac{\dot{\sigma_n} - \dot{p}}{\sigma_n - p} - \frac{v_0}{d_c}\right) \tag{6}$$

where the overdot defines the time derivative, and ξ is the radiation damping that serves as a proxy for the inertial term in the drained critical stiffness above. The frictional instability evolves with the effective stress, depending not only on the magnitude $((b-a)(\sigma_n - p)/d_c)$ and the rate of change in the effective stress $(-\alpha(\dot{\sigma_n} - \dot{p})/v_0)$, but also on changes in radiation damping $(\xi[(\dot{\sigma_n} - \dot{p})/(\sigma_n - p) - v_0/d_c])$. Therefore, if the stiffness of the loading system is less than a critical threshold value, the system will be unstable. Then, stick-slip may manifest as seismic slip, otherwise the system remains stable and fails aseismically. Thus, this condition can be used to discriminate between stable and unstable slip and the likelihood of quiescent slip or dynamic earthquakes.

2.4. Dilatant hardening

Finally, given these necessary and sufficient conditions for dynamic slip, i.e. strength, velocity-weakening, and critical stiffness, then dynamic slip can only develop if any dilatant hardening is insufficient to completely arrest the reactivation. Dilatant hardening is controlled by the rate of generation of pore pressures during shear compaction relative to their dissipation (Lockner and Byerlee, 1994; Segall and Rice, 1995; Yang and Dunham, 2022). This can be evaluated by a simple one-dimensional (1D) model for the simultaneous generation and dissipation of fluid pressures across a fault of thickness $\bar{a}$ and permeability k and conditioned by slip-induced changes in porosity ϕ (Samuelson et al., 2009). Fluid transfer across the fault is straightforwardly conditioned by pressure diffusion modulated by an internal fluid mass generation term f_D, representing a volume of fluid produced per unit fault volume.

Fluid mass generation and pressure diffusion across the fault can be written in dimensionless form as

$$\frac{\partial P_D}{\partial t_D} - \frac{\partial^2 P_D}{\partial x_D^2} = 0 \tag{7}$$

For Dietrich evolution, the following equation can be obtained:

$$f_D = \frac{1}{\ln\left(\frac{v_0}{v}\right)} V_D \left[\frac{-\left(\frac{v}{v_0} - 1\right)e^{-V_D t_D}}{1 + \left(\frac{v}{v_0} - 1\right)e^{-V_D t_D}}\right] \tag{8}$$

The non-dimensional parameters for pressure, time, relative location across the fault, and shear velocity are defined as

$$P_D = \frac{\phi}{\phi_\infty - \phi_0}\frac{p - p_0}{K_b} = \frac{\phi_0}{\varepsilon \ln\left(\frac{v_0}{v}\right)}\frac{p - p_0}{K_b} \tag{9}$$

$$t_D = ct/\bar{a}^2 \tag{10}$$

$$x_D = x/\bar{a} \tag{11}$$

$$V_D = v\bar{a}^2/cd_c \tag{12}$$

These, in turn, are defined in terms of the dimensional geometric parameters of layer half-width, $\bar{a}$, and the material property

of hydraulic diffusivity, c, as

$$c = \frac{k}{\eta} K_b \tag{13}$$

where K_b is the bulk modulus, η is the fluid viscosity, and k is the permeability. In addition, the pore pressure generation coefficient, ε (Samuelson et al., 2009), together with a state variable of final porosity, ϕ_∞, defines the response. Importantly, V_D controls the potential for dilatant hardening. This term can be alternately stated as the product of two individual dimensionless terms as

$$V_D = \frac{\bar{a}^2}{k} \frac{v\eta}{K d_c} \tag{14}$$

The first term of Eq. (14) refers to the drainage rate and the second to the undrained rate of pore pressure generation. For small V_D, drainage dissipates pore fluid pressures rapidly and the fault response is drained. Conversely, when V_D is large, the fault response is undrained. This switch (from drained to undrained response) occurs at $V_D \approx 1$. Non-dimensionalized pressure is the ratio of the current pore pressure to the peak undrained pressure at $t = 0$ and is bounded by $0 \le P_D \le 1$. This represents the spectrum of fully drained to undrained responses for a system initially at pressure, p_0. The full spectrum of response can thus be uniquely defined in terms of parameter sets:

$$P_D = F[V_D, t_D, x_D, v / v_0] \tag{15}$$

The undrained response can be defined as a subset of parameters as $P_D = F(V_D t_D, v/v_0)$, or alternately $P_D = F(vt/D_c, v/v_0)$. If drainage is suppressed for the undrained response, the dimensionless pressure evolves as

$$P_D = \ln\left\{\frac{v_0}{v}\left[1 + \left(\frac{v}{v_0} - 1\right)e^{-V_D t_D}\right]\right\} \Big/ \ln\left(\frac{v_0}{v}\right) \tag{16}$$

Importantly, the magnitude of dilatancy, as embodied in the pore pressure generation coefficient, ε, controls the dimensionless pressure, P_D. When drained, the peak pore pressure is centrally located within the fault at $x_D = 0$. Then, the evolution of the pore pressure can be followed with dimensionless displacement, $V_D t_D$, (Fig. 3a), or relative to time, t_D (Fig. 3b). The former can be used to follow the build-up of pore fluid pressure in the fault, and the latter to follow the dissipation. It is clear from these results that the parameter $V_D = v\bar{a}^2/(cd_c)$ acts as a drainage state term in delineating the transition between undrained and drained loading.

Thus, these four conditions define the potential for dynamic slip and its arrest, with the general considerations applying differently, but in equal measure, to rockbursts and gas outbursts.

3. Constraints on triggered seismicity

A variety of methods predict the expected peak magnitudes of injection-triggered earthquakes based on total injected volume (McGarr, 1976, 2014), size of the stimulated volume (Shapiro et al., 2007, 2011), fault mechanics and scaling (Galis et al., 2017), and probabilistic approaches involving seismicity rates (van der Elst et al., 2016). The main advantage of using the total injected volume alone as a threshold metric is that no additional *a priori* information is required to define the potential hazard. Such approaches (McGarr, 1976, 2014) assume that the maximum seismic moment (M_0^{max}) is limited by a threshold defined by the product of the injected volume (ΔV) and the intrinsic shear modulus (G), i.e. $M_0^{max} = G\Delta V$. However, recent earthquakes accidently triggered by fluid injection (Atkinson et al., 2016; Diehl et al., 2017; Kim et al., 2018) and those purposely reactivated on faults (Guglielmi et al., 2015) exhibit magnitudes well above this threshold. Controlling mechanisms remain unclear.

The pre-existing shear stress state is a key parameter that can control this response. The threshold for moment magnitude (McGarr, 1976, 2014) assumes an intermediate shear stress between peak strength and residual stress – midway in the window that defines stress drop for tectonic earthquakes (Fig. 4, inset at 50%). However, this ignores the possibility of recovering the "full" strain energy stored for a fault that is "teetering" close to failure (e.g. 99% in Fig. 4). We denote a stress ratio (c') within this window as the proportion of the full stress drop magnitude. An increase in pore pressure (Δp) triggers fault rupture as $\mu\Delta p = (1 - c')\Delta\tau$, where $\mu\Delta p$ is the shear strength resulting from the elevated pore pressure, and $(1 - c')\Delta\tau$ is the stress difference between the initial shear stress and the shear strength. Substituting $\Delta p = \Delta\tau/(2\mu)$ (Eq. (3), Galis et al., 2017), the maximum anticipated moment magnitude is defined as $M_0^{max} = G\Delta V/[2(1 - c')]$. This represents an increase in seismic moment ($c' > 50\%$) relative to an induced event ($c = 50\%$). This behavior accommodates events larger than the threshold $M_0^{max} = G\Delta V$ since the initial stress is midway in the stress drop window (Fig. 4, inset), but this respects all other constraints. In this case, failure occurs on the most critical plane with respect to the stress field and rupture is restricted to the contours of the

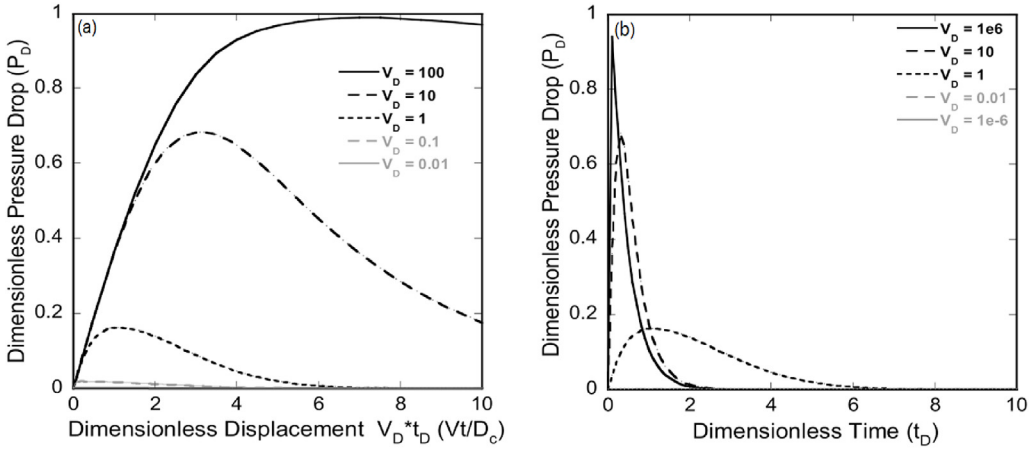

Fig. 3. (a) Evolution of pressure (P_D) with dimensionless displacement ($V_D t_D$) for variable drainage state (V_D). $V_D = 1$ acts as a threshold between undrained and drained behavior. (b) Pressure drop with dimensionless time (t_D). Note that curves for $V_D < 0.1$ are near congruent with the x-axis at $P_D < 0.02$ (after Samuelson et al., 2009).

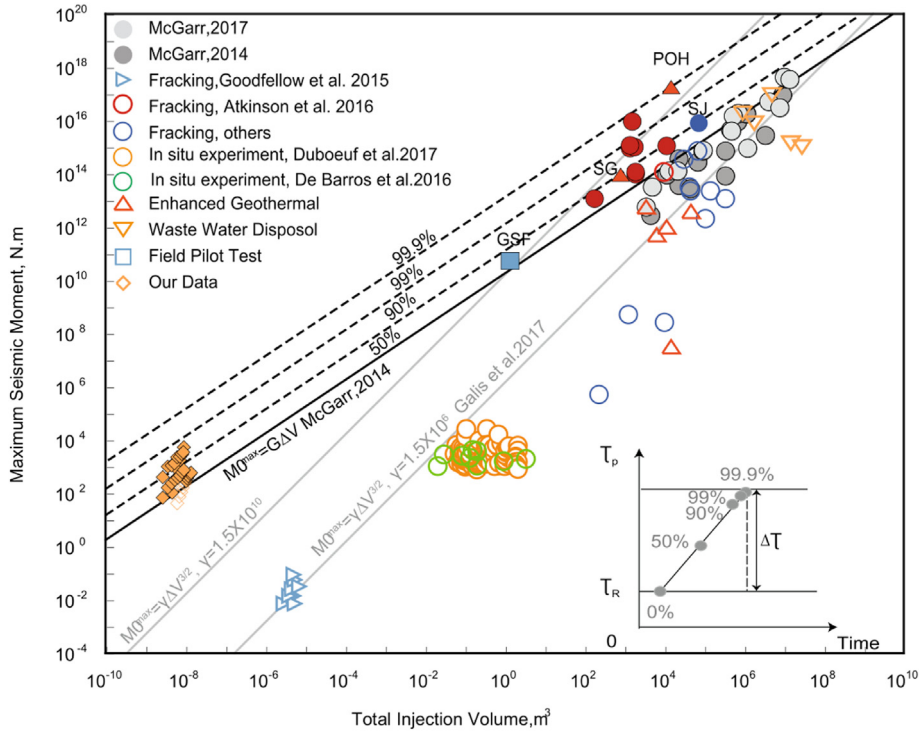

Fig. 4. Seismic moment versus total fluid volume for fluid injection-triggered earthquakes. The black solid line represents the upper threshold seismic moment for mean stress. The black dashed line denotes the thresholds for prestress defined in terms of c' values, as per the inset in the figure, using the characterization from Li et al. (2021). In contrast, the grey solid line represents the maximum seismic moment for runaway ruptures for two different γ values, where decreasing γ represents increasing prestress (Galis et al., 2017). Note that the seismic moment for the runaway rupture (Galis et al., 2017) scales as $M \propto \Delta V^{3/2}$ and decreases with increasing prestress and that the constrained rupture (Li et al., 2021) scales as $M \propto \Delta V$ and seismic moment increases with increasing prestress. POH=Pohang earthquake (Kim et al., 2018); SG = St. Gallen earthquake (Diehl et al., 2017); SJ = St. John earthquake (Mahani et al., 2017); GSF = Guglielmi reactivated fault (Guglielmi et al., 2015) (after Galis et al., 2017; Li et al., 2021).

pressurized reservoir, i.e. the rupture cannot run away dynamically. Failure is described by Byerlee's law ($\mu \approx 0.6$, absent cohesion), but no distinction is made between aseismic and seismic slip. These relations (obtained by both McGarr (1976, 2014) and Li et al. (2021)) match observations well.

These models (McGarr, 1976, 2014) evaluate the elastic strain energy within the pressurized volume, with failure restricted to that volume. The rupture cannot propagate outside the contour of that region. This results in a scaling relation as $M \propto \Delta V$. Physics-based models of rupture (Galis et al., 2017) can accommodate propagation outside the pressurized region. Here, shear failure again transits through a prestressed region, but is moderated by Mode II/III fracture toughness at the tip of the propagating rupture. This accommodates constrained, arrested, and runaway ruptures (Galis et al., 2017) parameterizing the scaling relation as $M \propto \Delta V^{3/2}$. The scaling of this model (Galis et al., 2017) is included in Fig. 4 for comparison. The assumptions in these models (McGarr, 1976; Galis et al., 2017) contrast, but both model outputs are broadly congruent with current observations for proposed M vs.ΔV relations within the range $2 < M < 6$. The importance of discriminating between these two behaviors for the M-ΔV relations is that the predictions diverge for larger injection volumes and hence larger seismic moments. This is particularly true for large injection volumes and earthquake magnitudes ($M > 4$), where predictions are larger for runaway faults (Galis et al., 2017) compared to constrained rupture. Unfortunately, field data do not discriminate within this range of field-scale observations ($2 < M < 6$), are absent for larger magnitudes ($M > 6$), and have only small-scale in situ experiments (Guglielmi et al., 2015; De Barros et al., 2016; Duboef et al., 2017) and laboratory observations (Goodfellow et al., 2015; Li et al., 2021) as scaling discriminants. Laboratory observations are potentially most useful for discriminating between the ΔV and $\Delta V^{3/2}$ moment-volume scaling relations (Fig. 4). These represent either constrained (McGarr, 1976, 2014) or unconstrained (Galis et al., 2017) ruptures within the fluid pressurized reservoir. The "constrained" only represents uniform fluid pressurization, uniform stress, spatially uniform shear displacement on the fault, and frictional strength – conditions typically replicated in experiments (Li et al., 2021). The "unconstrained" description represents rupture on a fault, again under a uniform prestress, but with both frictional resistance and Mode II fracture toughness at the fault tip/edge. This model (Galis et al., 2017) can be an analog to the driven fractures observed in experimental data (Goodfellow et al., 2015) in this particular case representing Mode I response. The strong fit of these two different models to their respective experimental geometries suggests their application at the field scale. The "constrained" model heuristically represents the geometry of broad pressurization on a weak fault. This can be considered as representing injection into a high permeability fault with zero or low fracture toughness or cohesion. Conversely, the "unconstrained" propagation model best represents a locally pressurized strong fault of low permeability (or rapidly pressurized) and with significant cohesion or fracture toughness. The distinct differences in the M-ΔV response for these two contrasting configurations, embodied in the two models, diminish with increasing injection volume and seismic moment as the two forms of scaling converge – before crossing and then ultimately diverging.

This intersection of the $M \propto \Delta V$ and $M \propto \Delta V^{3/2}$ scaling relations at intermediate seismic moments/injection volumes leaves the principal field-scale response modes unclear. However, the tectonic shear stress acting on the fault is a key property in defining the response. This is in addition to the frictional characteristics of the

fault and the stiffness of the reservoir. Fault friction is tightly constrained for real faults, as is reservoir stiffness, where the injected volume is typically known. Thus, the magnitude of the prestress remains an important parameter in characterizing the ultimate response.

This approach quantifies the role of pre-existing shear stress in defining the elevated seismic moment that can be recovered by fluid injection activities. Indeed, it directly explains the observation that the 2017 M_w 5.5 Pohang earthquake is so large for a relatively small volume of injected fluid (Fig. 4, POH) (Li et al., 2021).

4. Controls on permeability evolution

Triggered seismicity typically occurs as a result of the reactivation of pre-existing faults. This rupture creates new connected porosity and typically increases permeability. Thus, the distribution of seismicity can potentially be used to monitor fracture evolution and indeed changes in crustal permeability. Therefore, MEQs are coded with important details of the spatial distribution of transport properties. These include permeability evolution. This assumption is based on the possibility that MEQs result from shear remobilization based on an increase in pore pressure. The generation of MEQs herald the creation of porosity and associated permeability, the locations of which define the topology of the fracture network. For low-permeability crustal rocks, the permeability can increase by many orders of magnitude. Thus, changes in permeability are constrained if the energy release or other features of the MEQs are mechanistically linked to the creation of porosity and hence permeability. This link requires a physics-based connection between MQs, fracture displacement, and changes in fracture morphology (Fang et al., 2018; Ishibashi et al., 2018; Li et al., 2022; Yu et al., 2024).

It is possible to use high-fidelity filed data that include injectivity data and MEQ information from stimulations at EGS-Collab (Kneafsey et al., 2018) and UtahFORGE (McLennan et al., 2023). These are the cataloged results of in situ hydraulic injection data that increase permeability in the subsurface through high-pressure fluid injection. The EGS-Collab injection is completed from an adit 1500 m below the surface at the Sanford Underground Research Facility (SURF) — an underground laboratory for neutrino experiments in Lead, South Dakota, USA. The UtahFORGE injection is completed in a deviated borehole 2500 m below the surface as part of the Frontier Observatory for Research in Geothermal Energy (FORGE) in Milford, Utah, USA. The aim is to create new porosity and hence permeability. These represent the few sites where simultaneous observations of permeability evolution and MEQ histories are available — potentially linking observed changes in permeability to the quantitative MEQ record.

Observations of MEQs during injection (Fig. 5) show the propagation of the pressure pulse due to stimulation. This defines the outermost front of the propagating fluid pressure pulse and thus the external fluid pressure condition — assuming that the fractures are critically stressed and fail with an infinitesimal perturbation in the in situ conditions of elevated pore pressures and associated drop in effective stress. Injectivity is the ratio of injection rate to wellhead overpressure. Assuming steady flow, and defining the radius of either spherical or cylindrical flow domains by the advancing front of seismicity, injectivity can be converted into a true diagnostic property of the reservoir — permeability. The evolution of permeability over time is derived directly from these injectivity data as a complement to the time history of the MEQs (Fig. 6). Thus, the field-measured evolution of permeability and the seismic catalog are the two fundamental datasets that are available to link permeability to features of the MEQ record (i.e. seismic moment and location). As this seismicity–permeability relationship is unknown, we use machine learning to define it.

These simultaneous observations of MEQs and local permeability generation define a framework for predicting permeability evolution. A bidirectional long short-term memory (Bi-LSTM) neural network is utilized (Schuster and Paliwal, 1997; Hochreiter and Schmidhuber, 1997). The aim is to predict permeability evolution (as model output) from MEQ features (as input features). The input features are the seismicity rate, λ_i, and the logarithm of the cumulative seismic moment, $\mathscr{M}_i$. These are all extracted from the EGS-Collab and UtahFORGE datasets. The models are first evaluated for each dataset, and then the generalizability of the model across the two datasets is examined through transfer learning.

A Bi-LSTM structure can be used to predict permeability changes based on MEQ features. For this dataset, the best-performing model contains two hidden layers, each with 64 nodes. This represents a batch size of 96 and a learning rate of 0.001 over 150 epochs. The Utah FORGE Bi-LSTM model provides high-fidelity fits across all training, validation, and testing sets (Fig. 7). The R^2 value is only 0.85, but the final permeability is still close to the observed value. The poorer performance on the test set (Stage 3) may be because the model trained in Stage 1 may have different features to the hydraulic stimulation employed between these two stages. Stage 1 stimulated the open hole section of the wellbore, whereas Stage 3 was in the perforated interval. Also, different working fluids used in these multiple stages (McLennan et al., 2023) may contribute to particular patterns in permeability evolution.

This identical workflow can be used for the EGS-Collab data — a similar but smaller volume injection experiment conducted at a site about 1000 km away, i.e. using the injectivity data to define the

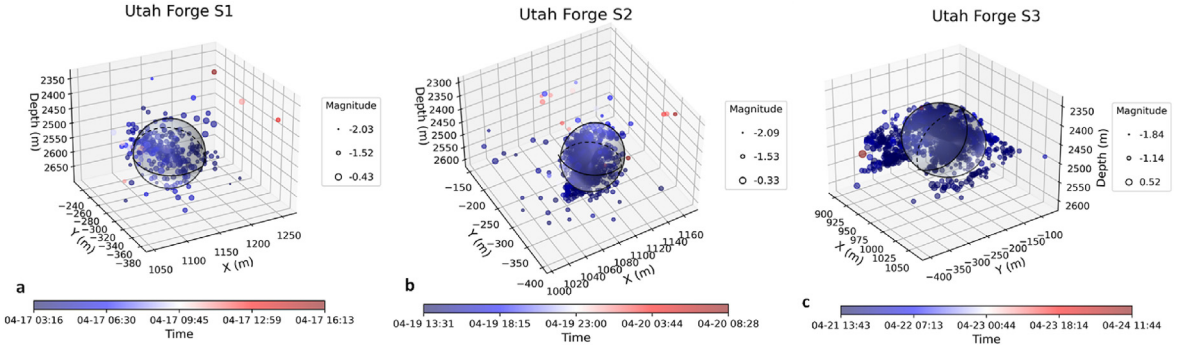

Fig. 5. Magnitude, location, and timing of MEQs for UtahFORGE stimulations for Stages 1–3 (S1–S3). Event timing is shown in color with magnitude scaled by radius. Moment magnitude (M) ranges from 2.09 to 0.52. Note the general spherical form of the migrating seismicity (after Yu et al., 2024) and the spherical form of the assumed migration of fluids from the injection perforation.

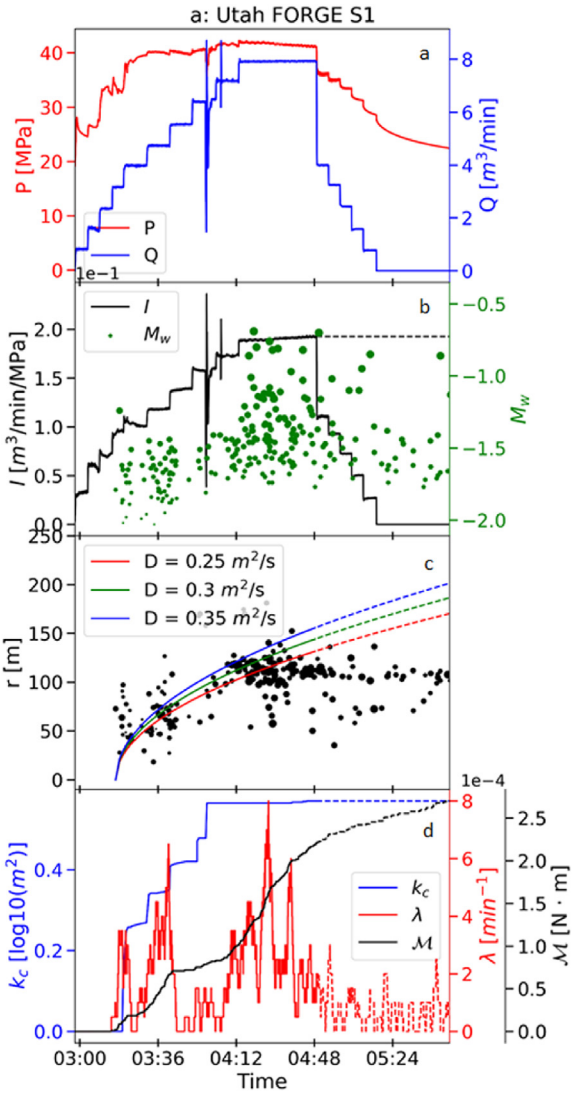

Fig. 6. Results of injection and associated seismicity observations for Stage 1 (hydraulic stimulation) at UtahFORGE. (a) Evolution of injection pressure (p) with injection rate (Q); (b) Injectivity time history (I) vs. MEQ moment magnitude (M_w); (c) Radius to outer pressure (r) fit to seismicity front (Shapiro et al., 1997, 2002) and used in the evaluation of steady-state permeability; and (d) Permeability change (k_c) and change in two MEQ features (logarithm of cumulative seismic moment ($\mathcal{M}$) and seismicity rate (λ)) (after Yu et al., 2024).

permeability evolution and match it to the seismicity catalog. Again, applying the same machine learning algorithm to three successive injection episodes for training, validation, and then testing provides as good predictions of permeability evolution as for the UtahFORGE data in Fig. 7. These are apparent for Episodes 3–5 in Fig. 5 of Yu et al., 2024), but are not shown here. We note that the ultimate predictions of permeability are almost exact (Fig. 7), but the time histories deviate on the path to the final predicted permeability. The stimulation periods are short (~2 h) and the principal interest is how the permeability is increased at the end of the stimulation. For all machine learning fits, the permeability data are continuous, but the seismic data are discrete and require to be binned with time. Therefore, changes in injection rates or the use of different viscosity fluids may impact this result. However, the time histories are remarkable in their precision, given that the prediction of permeability is purely from the MEQ data.

A final question is whether this scaling of permeability change to cumulative seismic moment is universal across tectonic and stratigraphic sections. This can be tested using transfer learning. We evaluate the generalizability of the models across datasets. Specifically, the UtahFORGE model using Bi-LSTM is used to predict another dataset — the EGS-Collab data, and vice versa.

The EGS-Collab Bi-LSTM model can be used to successfully transfer data (Yu et al., 2024) to the UtahFORGE dataset (Fig. 8). These transfer learning models can predict the ultimate permeability of the hydraulic stimulations, details of which are provided in the supplemental information for Yu et al. (2024). The observed success in applying the transfer learning suggests the domain independence and generalizability of the extracted MEQ features in estimating the change in permeability. This suggests the establishment of a robust physical link with causality that may exist between the release of strain energy indexed by cumulative MEQ magnitude and the creation of porosity/permeability. Typically, however, the accuracy of the model prediction may be limited by the quality of the dataset. This is particularly true for datasets that necessitate simultaneous measurements of accurate MEQ locations from high-resolution seismic networks, together with local measurements of fluid injection pressures and volumes.

Although the one-to-one correspondence between permeability and the cumulative seismic moment is evident from the ML correlation (Fig. 8), there is no indication of this causality, which can be recovered by noting that change in permeability (Δk) is directly related to the change in aperture ($\Delta\bar{a}$) in fractured media as $\Delta k \propto (\Delta\bar{a})^3$. Similarly, the change in aperture in the shear reactivation of dilating fractures is proportional to the product of the dilation angle ($\tan i$) and the fault slip of shear offset (u_s) as $\Delta\bar{a} = u_s \tan i$. Since the seismic moment is proportional to the fault slip displacement as $M \propto u_s$, the change in permeability can be linearly related to the seismic moment. This is discussed in detail for the interested reader in Yu et al. (2024).

5. Conclusions

Triggered seismicity has become an important consideration in contemporary resource recovery projects, particularly those related to the recovery and storage of energy and fuels in the subsurface. Triggered events can be large ($M_w > 6$) and hazardous, and indeed can limit projects due to their occurrence. The mode of rupture — dynamic vs. quiescent — is controlled by four interacting characteristics — strength, second-order frictional effects including velocity weakening response, stiffnesses of the geological environment, and the absence of damping effects such as dilatant hardening. A framework for this response is enumerated, which applies equally to rockbursts and dynamic gas outbursts — again relying on the concepts of rupture stability and energy release rates.

The very large magnitudes of some damaging earthquakes that result from only modest perturbations of subsurface conditions by limited magnitudes of pore fluid pressures or volumes can be best understood in terms of critically stressed reservoirs. Here, modest overpressures in critically stressed media can recover significant magnitudes of tectonic strain energy accumulated over long interseismic periods. Such concepts readily explain energy release in terms of seismic moments that are many orders of magnitude larger than those anticipated from the small perturbations to the reservoir. Such models scale increasing moment release with increasing critical stress magnitudes for rigid faults and with rupture contained within the pressurized region and provide an excellent analog for observations.

The triggering of such MEQs is an intrinsic consequence of the injection of stimulation fluids into the subsurface and is typically employed to develop associated porosity with the ultimate goal of

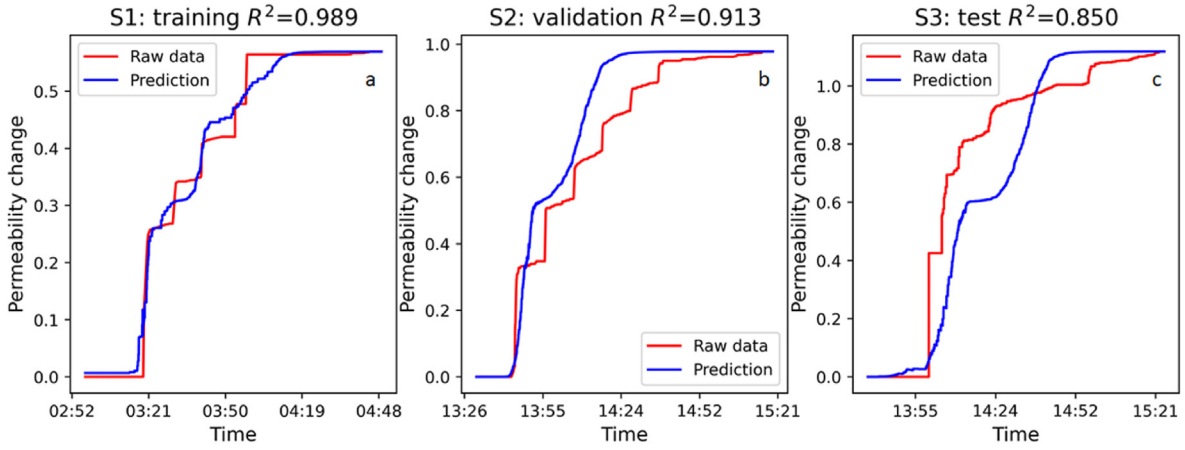

Fig. 7. Comparison of raw permeability data for ground truth with predictions from training, validation, and testing for UtahFORGE. Predictions from the UtahFORGE Bi-LSTM model were contrasted with the original data using (a) Stage 1 for training, (b) Stage 2 for validation, and (c) Stage 3 for testing. Note that Stages 1, 2, and 3 occur on successive days (see timestamps in Fig. 5) (after Yu et al., 2024).

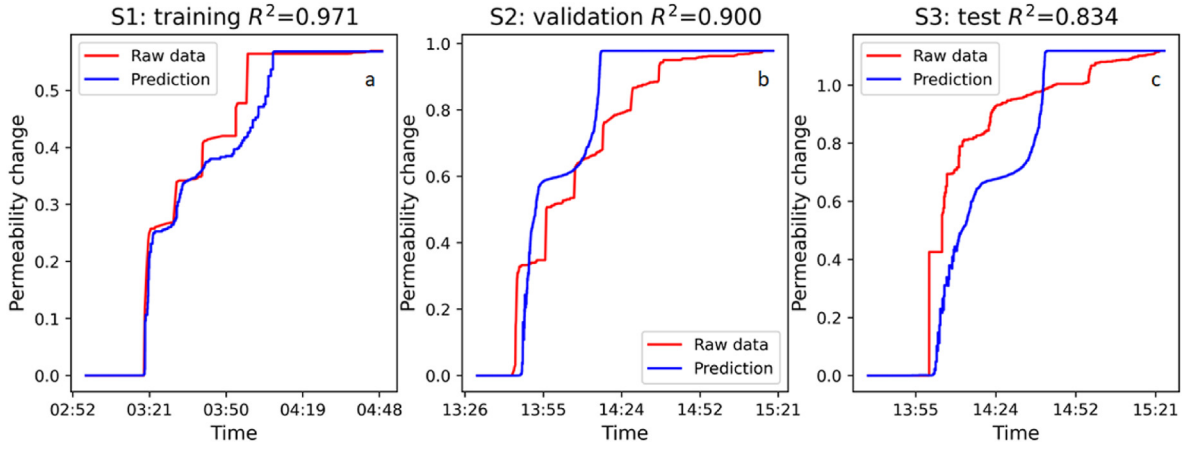

Fig. 8. Ground truth and transfer learning predictions for UtahFORGE. Results of transfer learning applied to the Utah FORGE dataset results using the EGS Collab Bi-LSTM model. Note that the predictions are excellent, even for the transfer learning (after Yu et al., 2024).

increasing permeability. Indeed, such creation of porosity is illuminated by the MEQs that produce the porosity gain, suggesting that MEQs can in turn be used as a diagnostic of the change in permeability. Machine learning models are shown to be capable of defining links between permeability and seismicity if the appropriate parameters and processes can be understood. Well-constrained experiments, where permeability evolution and time histories of MEQs are available, are required to populate such models and constrain relations. The change in permeability can be shown to scale with cumulative seismic moment, thus enabling the recovery of permeability evolution from the seismic record as a diagnostic characteristic.

Such physics-based methods for understanding triggered seismicity and relating permeability evolution to seismicity hold promise for improved control and safer utilization of the subsurface, as an important source and repository for energy, fuels, and other critical resources.

CRediT authorship contribution statement

Derek Elsworth: Writing – review & editing, Writing – original draft, Supervision, Methodology, Funding acquisition, Formal analysis, Conceptualization. **Ziyan Li:** Writing – review & editing, Writing – original draft, Methodology, Investigation, Formal analysis. **Pengliang Yu:** Writing – review & editing, Writing – original draft, Validation, Methodology, Formal analysis, Conceptualization. **Mengke An:** Writing – review & editing, Writing – original draft, Validation, Investigation, Formal analysis. **Fengshou Zhang:** Writing – review & editing, Writing – original draft, Project administration, Investigation, Formal analysis, Conceptualization. **Rui Huang:** Writing – review & editing, Writing – original draft, Methodology, Investigation, Formal analysis. **Zihan Sun:** Writing – review & editing, Writing – original draft, Validation, Methodology, Investigation, Formal analysis, Conceptualization. **Guanglei Cui:** Writing – review & editing, Writing – original draft, Supervision, Project administration, Methodology, Formal analysis, Conceptualization. **Tianyu Chen:** Writing – review & editing, Writing – original draft, Methodology, Investigation. **Quan Gan:** Writing – review & editing, Writing – original draft, Methodology, Funding acquisition, Formal analysis, Conceptualization. **Yixin Zhao:** Writing – review & editing, Writing – original draft, Investigation, Funding acquisition, Formal analysis. **Jishan Liu:** Writing – review & editing, Writing – original draft, Methodology, Investigation, Funding acquisition, Formal analysis. **Shimin Liu:** Writing – review & editing, Validation, Investigation, Funding acquisition, Formal analysis.

Declaration of competing interest

The authors declare that they have no known competing financial interests or personal relationships that could have appeared to influence the work reported in this paper.

Acknowledgements

Derek Elsworth acknowledges the support from a Gledden Visiting Fellowship from the Institute of Advanced Studies at the University of Western Australia, Australia, and the G. Albert Shoemaker Endowment at Pennsylvania State University, USA.

References

Alghannam, M., Juanes, R., 2020. Understanding rate effects in injection-induced earthquakes. Nat. Commun. 11, 3053.
An, M., Zhang, F., Min, K.B., Elsworth, D., He, C., Zhao, L., 2022. Frictional stability of metamorphic epidote in granitoid faults under hydrothermal conditions and implications for injection-induced seismicity. J. Geophys. Res. Solid Earth 127, e2021JB023136.
Atkinson, G.M., Eaton, D.W., Ghofrani, H., et al., 2016. Hydraulic fracturing and seismicity in the western Canada sedimentary basin. Seismol Res. Lett. 87, 631–647.
Bao, X., Eaton, D.W., 2016. Fault activation by hydraulic fracturing in western Canada. Science 354, 1406–1409.
Candela, T., Wassing, B., ter Heege, J., Buijze, L., 2017. How earthquakes are induced. Science 360, 598–600.
Cueto-Felgueroso, L., Vila, C., Santillán, D., Mosquera, J.C., 2018. Numerical modeling of injection-induced earthquakes using laboratory-derived friction laws. Water Resour. Res. 54 (12), 9833–9859.
De Barros, L., Daniel, G., Guglielmi, Y., et al., 2016. Fault structure stress, or pressure control on the seismicity in shale? Insights from a controlled experiment of fluid-induced fault reactivation. J. Geophys. Res. 121, 4506–4522.
Diehl, T., Kraft, T., Kissling, E., Wiemer, S., 2017. The induced earthquake sequence related to the St. Gallen deep geothermal project (Switzerland): fault reactivation and fluid interactions imaged by microseismicity. J. Geophys. Res. Solid Earth 122, 7272–7290.
Dieterich, J.H., 1979. Modeling of rock friction: 1. Experimental results and constitutive equations. J. Geophys. Res. 84 (B5), 2161.
Duboef, L., De Barros, L., Cappa, F., Guglielmi, Y., Deschamps, A., Seguy, S., 2017. Aseismic motions drive a sparse seismicity during fluid injections into a fractured zone in a carbonate reservoir. J. Geophys. Res. 122, 8285–8304.
Ellsworth, W.L., 2013. Injection-induced earthquakes. Science 341 doi.org/1225942.
Elsworth, D., Spiers, C.J., Niemeijer, A.R., 2016. Understanding induced seismicity. Science 354, 1380–1381.
Fang, Y., Elsworth, D., Cladouhos, T.T., 2018. Reservoir permeability mapping using microearthquake data. Geothermics 72, 83–100.
Foulger, G., Wilson, M., Gluyas, J., Julian, B., Davies, R., 2018. Global review of human-induced earthquakes. Earth Sci. Rev. 178, 438–514.
Galis, M., Ampuero, J.P., Mai, P.M., Cappa, F., 2017. Induced seismicity provides insight into why earthquake ruptures stop. Sci. Adv. 3 doi.org/aap.7528.
Goodfellow, S.D., Nasseri, M.H.B., Maxwell, S.C., Young, R.P., 2015. Hydraulic fracture energy budget: insights from the laboratory. Geophys. Res. Lett. 42, 3179–3187.
Grandin, R., Vallée, M., Lacassin, R., 2017. Rupture process of the Mw 5.8 Pawnee, Oklahoma, earthquake from Sentinel-1 InSAR and seismological data. Seismol Res. Lett. 88, 994–1004.
Grigoli, F., Cesca, S., Rinaldi, A.P., et al., 2018. The November 2017 M_w 5.5 Pohang earthquake: a possible case of induced seismicity in South Korea. Science 360, 1003–1006.
Gu, J.C., Rice, J.R., Ruina, A.L., Tse, S.T., 1984. Slip motion and stability of a single degree of freedom elastic system with rate and state dependent friction. J. Mech. Phys. Solid. 32 (3), 167–196.
Guglielmi, Y., Cappa, F., Avouac, J.P., Henry, P., Elsworth, D., 2015. Seismicity triggered by fluid injection-induced aseismic slip. Science 348, 1224–1226.
Hochreiter, S., Schmidhuber, J., 1997. Long short-term memory. Neural Comput. 9 (8), 1735–1780.
Horton, S., 2012. Disposal of hydrofracking waste fluid by injection into subsurface aquifers triggers earthquake swarm in Central Arkansas with potential for damaging earthquake. Seismol Res. Lett. 83, 250–260.
Hunfeld, L.B., Chen, J., Hol, S., Niemeijer, A.R., Spiers, C.J., 2020. Healing behavior of simulated fault gouges from the Groningen gas field and implications for induced fault reactivation. J. Geophys. Res. Solid Earth 125 (7), e2019JB018790.
Im, K., Elsworth, D., Fang, Y., 2018. The influence of preslip sealing on the permeability evolution of fractures and faults. Geophys. Res. Lett. 45 (1), 166–175.
Ingebritsen, S.E., Manning, C.E., 2010. Permeability of the continental crust: dynamic variations inferred from seismicity and metamorphism. Geofluids 10 (1–2), 193–205.
Ishibashi, T., Elsworth, D., Fang, Y., Riviere, J., Madara, B., Asanuma, H., Watanabe, N., Marone, C., 2018. Friction-stability-permeability evolution of a fracture in granite. Water Resour. Res. 54 (12), 9901–9918.
Keranen, K.M., Savage, H.M., Abers, G.A., Cochran, E.S., 2013. Potentially induced earthquakes in Oklahoma, USA: links between wastewater injection and the 2011 M_w 5.7 earthquake sequence. Geology 41, 699–702.
Kim, K.H., Ree, J.H., Kim, Y., Kim, S., Kang, S.Y., Seo, W., 2018. Assessing whether the 2017 Mw5.4 Pohang earthquake in South Korea was an induced event. Science 360, 1007–1009.
Kneafsey, T.J., Dobson, P., Blankenship, D., et al., 2018. An overview of the EGS Collab project: field validation of coupled process modeling of fracturing and fluid flow at the Sanford Underground Research Facility. In: Proceedings of the 43rd Workshop on Geothermal Reservoir Engineering. Stanford University, Stanford, USA.
Li, Z., Elsworth, D., Wang, C., 2021. Constraining maximum event magnitude during injection-triggered seismicity. Nat. Commun. 12, 1528.
Li, Z., Elsworth, D., Wang, C., 2022. Induced microearthquakes predict permeability creation in the brittle crust. Front. Earth Sci. 10. https://doi.org/10.3389/FEART.2022.1020294.
Lockner, D.A., Byerlee, J.D., 1994. Dilatancy in hydraulically isolated fault and the supression of instability. Geophys. Res. Lett. 21, 2353–2356.
Mahani, A.B., Schultz, R., Kao, H., Walker, D., Johnson, J., Salaset, C., 2017. Fluid injection and seismic activity in the Northern Montney Play, British Columbia, Canada, with special reference to the 17 August 2015 M_w 4.6 induced earthquake. Bull. Seismol. Soc. Am. 107, 542–552.
Majer, E.L., Baria, R., Stark, M., Oates, S., Bommer, J., Smith, B., Asanuma, H., 2007. Induced seismicity associated with enhanced geothermal systems. Geothermics 36 (3), 185–222.
Manga, M., Beresnev, I., Brodsky, E.E., Elkhoury, J.E., Elsworth, D., Ingebritsen, S.E., Mays, D.C., Wang, C.Y., 2012. Changes in permeability caused by transient stresses: field observations, experiments, and mechanisms. Rev. Geophys. 50 (2). https://doi.org/10.1029/2011RG000382.
Manning, C.E., Ingebritsen, S.E., 1999. Permeability of the continental crust: implications of geothermal data and metamorphic systems. Rev. Geophys. 37 (1), 127–150.
McClure, M.W., Horne, R.N., 2014. An investigation of stimulation mechanisms in enhanced geothermal systems. Int. J. Rock Mech. Min. Sci. 72, 242–260.
McGarr, A., 1976. Seismic moment and volume changes. J. Geophys. Res. 81, 1487–1494.
McGarr, A., 2014. Maximum magnitude earthquakes induced by fluid injection. J. Geophys. Res. Solid Earth 119 (2), 1008–1019.
McGarr, A., Barbour, A.J., 2017. Wastewater disposal and the earthquake sequences during 2016 near Fairview, Pawnee, and Cushing. Oklahoma. Geophys. Res. Lett. 44, 9330–9336.
McGarr, A., Simpson, D., Seeber, L., 2002. 40 Case histories of induced and triggered seismicity. Int. Geophys. 81, 647–661.
McLennan, J., England, K., Rose, P., Moore, J., Barker, B., 2023. Stimulation of a high-temperature granitic reservoir at the Utah FORGE Site. In: SPE Hydraulic Fracturing Technology Conference and Exhibition. The Woodlands, USA. https://doi.org/10.2118/212346-MS.
Olsen, M.P., Scholz, C.H., Léger, A., 1998. Healing and sealing of a simulated fault gouge under hydrothermal conditions: implications for fault healing. J. Geophys. Res. Solid Earth 103 (B4), 7421–7430.
Pearson, C., 1981. The relationship between microseismicity and high pore pressures during hydraulic stimulation experiments in low permeability granitic rocks. J. Geophys. Res. Solid Earth 86 (B9), 7855–7864.
Rice, J.R., 1993. Spatio-temporal complexity of slip on a fault. J. Geophys. Res. Atmos. 98 (B6), 9885–9907.
Ruina, A., 1983. Slip instability and state variable friction laws. J. Geophys. Res. Solid Earth 88 (B12), 10359–10370.
Samuelson, J., Elsworth, D., Marone, C., 2009. Shear-induced dilatancy of fluid-saturated faults: experiment and theory. J. Geophys. Res. 114, B12404.
Schuster, M., Paliwal, K.K., 1997. Bidirectional recurrent neural networks. IEEE Trans. Signal Process. 45 (11), 2673–2681.
Segall, P., Rice, J.R., 1995. Dilatancy, compaction, and slip instability on a fluid-infiltrated fault. J. Geophys. Res. 100 (B11), 22155–22171.
Shapiro, S.A., Dinske, C., 2009. Fluid-induced seismicity: pressure diffusion and hydraulic fracturing. Geophys. Prospect. 57, 301–310.
Shapiro, S.A., Huenges, E., Borm, G., 1997. Estimating the crust permeability from fluid-injection-induced seismic emission at the KTB site. Geophys. J. Int. 131 (2), 15–23.
Shapiro, S.A., Rothert, E., Rath, V., Rindschwentner, J., 2002. Characterization of fluid transport properties of reservoirs using induced microseismicity. Geophysics 67 (1), 212–220.
Shapiro, S.A., Dinske, C., Kummerow, J., 2007. Probability of a given-magnitude earthquake induced by a fluid injection. Geophys. Res. Lett. 34 (22). https://doi.org/10.1029/2007GL031615.
Shapiro, S.A., Krüger, O.S., Dinske, C., Langenbruch, C., 2011. Magnitudes of induced earthquakes and geometric scales of fluid-stimulated rock volumes. Geophysics 76, 1ND–Z148.
Sun, Z., Elsworth, D., Cui, G., Li, Y., Zhu, A., Chen, T., 2024. Impacts of rate of change in effective stress and inertial effects on fault slip behavior: new insights into injection-induced earthquakes. J. Geophys. Res. 129, e2023JB027126.
van der Elst, N.J., Page, M.T., Weiser, D.A., Goebel, T.H.W., Hosseini, S.M., 2016.

Induced earthquake magnitudes are as large as (statistically) expected. J. Geophys. Res. Solid Earth 121, 4575–4590.
Walsh, F.R., Zoback, M.D., 2015. Oklahoma's recent earthquakes and saltwater disposal. Sci. Adv. 1 doi.org/1500195.
Westaway, R., Burnside, N.M., 2019. Fault "corrosion" by fluid injection: a potential cause of the November 2017 M_w 5.5 Korean earthquake. Geofluids 2019. https://doi.org/10.1155/2019/1280721.
Yang, Y., Dunham, E., 2022. Effect of porosity and permeability evolution on injection-induced aseismic slip. J. Geophys. Res. 126, e2020JB021258.
Yasuhara, H., 2004. Evolution of permeability in a natural fracture: significant role of pressure solution. J. Geophys. Res. 109 (B3), 3204.
Yeck, W.L., Hayes, G.P., McNamara, D.E., Rubinstein, J.L., Barnhart, W.D., Earle, P.S., Benz, H.M., 2016b. Oklahoma experiences largest earthquake during ongoing regional wastewater injection hazard mitigation efforts. Geophys. Res. Lett. 44, 198–207.
Yeck, W.L., Weingarten, M., Mcnamara, D., Bergman, E.A., 2016a. Far-field pressurization likely caused one of the largest injection induced earthquakes by reactivating a large preexisting basement fault structure. Geophys. Res. Lett. 43, 10198–10207.
Yu, P., Mali, A., Velaga, T., et al., 2024. Crustal permeability generated through microearthquakes is constrained by seismic moment. Nat. Commun. 15, 2057.

Derek Elsworth is the G. Albert Shoemaker Chair and Professor of Energy and Mineral Engineering and Geosciences at Pennsylvania State University, USA. His research interests are in the areas of computational mechanics, geomechanics and geophysics with applications to induced seismicity, and the related evolution in the mechanical and transport characteristics of fractured rocks with applications to geothermal energy, the deep geological sequestration of radioactive wastes and CO_2, and the storage and production of hydrogen and unconventional hydrocarbons, including coal–gas, tight gas–shales and hydrates, and instability and eruption dynamics of volcanoes.